AIAA JOURNAL
Vol. 46, No. 9, September 2008

Numerical Simulation of Two-Dimensional Blade-Vortex Interactions Using Finite Difference Lattice Boltzmann Method

Akinori Tamura,* Michihisa Tsutahara,† and Takeshi Kataoka‡
Kobe University, Hyogo 657-8501, Japan
and
Takashi Aoyama§ and Choongmo Yang¶
Japan Aerospace Exploration Agency, Tokyo 182-8522, Japan

DOI: 10.2514/1.30964

An unsteady two-dimensional inviscid blade-vortex interaction has been calculated using the finite difference lattice Boltzmann method of the compressible Euler model. The perturbed discrete Boltzmann equation based on a prescribed vortex approach has been proposed to prevent a vortex from diffusing by numerical dissipation. The discretization of the governing equation is based on a second-order-accurate explicit Runge–Kutta time integration and a fifth-order-accurate upwind scheme that includes additional terms to capture the shock waves clearly. Subsonic and transonic flows around an airfoil were simulated to validate the perturbed discrete Boltzmann equation system. The numerical results were compared with other numerical data, and good agreement has been obtained. In the simulation of the transonic blade-vortex interaction, an instantaneous pressure coefficient, a time history of a lift coefficient, and patterns of acoustic waves were compared with other numerical results, and were found to agree with them very well. We have also investigated a generation mechanism of acoustic wave caused by the blade-vortex interaction, the effect of the flow Mach number, and the influence of the vortex miss distance.

Nomenclature

A	=	positive constant that represents negative viscosity
a	=	core radius of the vortex
b	=	constant associated with the specific-heat ratio
c	=	chord length
$c_{i\alpha}$	=	particle velocity vector
c_s	=	sound speed
c_1, c_2	=	magnitude of the particle velocity
e	=	internal energy
e_0	=	internal energy of the rest fluid
f_i	=	velocity distribution function
f_i^{eq}	=	equilibrium distribution function
M	=	Mach number
M_{local}	=	local Mach number
p	=	pressure
p_0	=	pressure of the steady state without the vortex
r	=	radial distance from the vortex center
t	=	time
U	=	moving speed of the airfoil
u_α	=	flow velocity vector
V_α	=	grid velocity vector
v_θ	=	tangential velocity distribution of the vortex
X_v	=	X component of the relative distance between the vortex center and the leading edge
x_α	=	Cartesian coordinates
Y_v	=	vortex miss distance
α_0	=	angle of attack
Γ	=	vortex strength
γ	=	specific-heat ratio
Δp	=	fluctuation pressure
Δt	=	time step
Δu_α	=	relative velocity between the flow velocity and the moving speed of the airfoil
η_i	=	variable that controls the specific-heat ratio
η_0	=	magnitude of η_i
κ	=	variable that controls the numerical dissipation
Λ	=	intersection angle
ξ_α	=	generalized coordinates
ρ	=	density
ρ_0	=	density of the rest fluid
τ	=	positive constant that controls the strength of the dissipative effect
ϕ	=	relaxation time

Subscripts

i	=	direction of the particle velocity
j	=	grid point number
n	=	normal component to the boundary
P	=	remaining part of the total solution
t	=	tangential component to the boundary
V	=	prescribed part of the total solution
α	=	space direction of the Cartesian coordinates

Received 12 March 2007; revision received 23 November 2007; accepted for publication 21 May 2008.

*Doctoral Candidate, Graduate School of Science and Technology, 1-1, Rokkodaicho, Nada, Kobe. Student Member AIAA.

†Professor, Graduate School of Science and Technology, 1-1, Rokkodaicho, Nada, Kobe. Senior Member AIAA.

‡Associate Professor, Graduate School of Science and Technology, 1-1, Rokkodaicho, Nada, Kobe.

§Section Leader, Institute of Aerospace Technology, 7-44-1, Jindaijihigashi-machi, Chofu. Senior Member AIAA.

¶Researcher, Institute of Aerospace Technology, 7-44-1, Jindaijihigashi-machi, Chofu.

I. Introduction

BLADE-VORTEX interaction (BVI), which is a typical unsteady flow phenomena of a helicopter rotor, occurs when the trailing tip vortex shed from one blade interacts with both itself and the other blades in descending flight or maneuvers, especially during an approach to a landing. The BVI phenomena induces unsteady aerodynamic blade loading resulting in aeroelastic instabilities and blade vibrations, and also causes a highly directional impulsive noise. The BVI noise prevents a helicopter from being widely used as a means of intercity transportation in densely populated areas. Thus, this aeroacoustic problem has received considerable attention in the helicopter industry.

Generally, the problem of BVI can be viewed as unsteady and three-dimensional frames. Figure 1a shows the general BVI problem, which is an unsteady, three-dimensional close encounter of a curved line vortex at an arbitrary intersection angle, Λ. Under certain flight conditions, a blade can encounter a trailing tip vortex that is almost parallel to the blade, that is, $\Lambda = 0$. In this case, the interaction can be approximated to be two-dimensional but unsteady. Such a problem can be modeled as the interaction of an infinitely long line vortex with an infinitely long blade parallel to the line vortex. The schematic diagram of two-dimensional BVI is shown in Fig. 1b. We investigate this particular BVI problem and the aeroacoustic problem in this paper.

Experimental studies of a two-dimensional BVI have been carried out by several researchers [1–3]. Booth [1] modeled the parallel BVI by placing an airfoil downstream of an oscillating airfoil that generates discrete vortices. He provided the experimental results such as vortex trajectory data, vortex convection velocity, and acoustic pressure at low Mach number conditions. Kalkhoran and Wilson [2] carried out the unsteady vortex-interaction experiments at transonic Mach numbers ranging from 0.7 to 0.85, and concluded that the interaction between a vortex and an airfoil shock wave is significant for the transonic BVI but that the effect of the Reynolds number variation is small. Lee and Bershader [3] investigated a parallel head-on BVI and its noise generation mechanism in experimental and computational studies. They showed that the viscous effect plays a significant role in the head-on BVIs.

Several papers associated with the numerical simulation of BVI problems have been also provided. In the numerical simulation of the BVI phenomena, there are some difficulties; the most prominent is the numerical dissipation of the vortex, which prevents the preservation of the strength of the vortices, in particular, at the region where the grid resolution is not high enough. To resolve this difficulty, a solution procedure based on a perturbation method has been proposed by many researchers. Srinivasan et al. [4–6] developed a procedure for solving BVI problems using the Euler and thin-layer Navier–Stokes equations. Their approach, called the prescribed vortex method or the vortex embedded method, is based on the perturbation method wherein the dependent flow variables are divided into a prescribed part that defines the vortical disturbance and a remaining part that is obtained from the solution of the governing equations. Damodaran and Caughey [7] proposed a numerical procedure based on velocity-field decomposition that is similar to the prescribed vortex method proposed by Srinivasan et al. [4–6]. In their approach, the total velocity field is decomposed into two parts to prevent a vortex diffusion. The first part is an induced velocity field of the vortex and the second part is the difference between the total velocity and the vortex-induced velocity. This second part is unknown and is obtained from the solution of the governing equations. They numerically analyzed an unsteady inviscid transonic BVI and provided several numerical data. To capture acoustic signals caused by the BVI, a higher-order-accurate scheme is required. Wie et al. [8] proposed a computational aeroacoustics (CAA) solver that is developed by combining a prescribed vortex method with an optimized high-order-accurate compact (OHOC) scheme. They calculated the two-dimensional BVI and then provided not only an instantaneous pressure coefficient and a time history of lift coefficient, but also patterns of acoustic waves. However, it is well known that compact schemes need more computational time than explicit upwind schemes. A solution-adaptive mesh procedure [9,10] is an alternative approach to relieve the difficulty associated with the numerical dissipation of a vortex. This approach is required for the calculation of strong interactions, such as vortex-airfoil collisions, that can not be solved by a perturbation method. Oh et al. [10] investigated transonic BVI problems and the vortex-airfoil collision problem by using an unstructured adaptive mesh approach. The solution-adaptive mesh approach is a promising numerical method, but its algorithm tends to become complicated due to a mesh adaptation procedure.

On the other hand, the lattice Boltzmann method (LBM) [11–22] has become very powerful tool of computational fluid dynamics (CFD). A governing equation of the LBM is the lattice Boltzmann

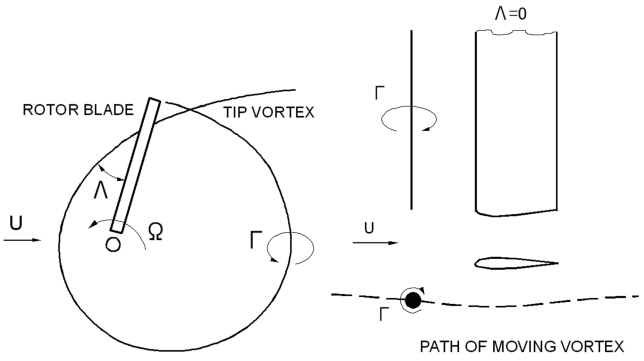

a) b)

Fig. 1 Schematic representation of a helicopter blade-vortex interaction and a particular case under certain flight conditions (from [7]): a) unsteady and three-dimensional blade-vortex interaction at an arbitrary intersection angle Λ, and b) parallel blade-vortex interaction with the limit of $\Lambda = 0$.

equation, which has complicated collision processes. Qian et al. [11] and Chen et al. [12] proposed the lattice Bhatnagar–Gross–Krook (BGK) collision operator, which simplifies the collision processes. Use of the lattice BGK model makes the computations more efficient and the transport coefficients can be simply described. Chen and Doolen [13] presented an overview that the LBM is not only computationally comparable with traditional numerical methods, but also easy to program and to include new physics because of the simple form of the governing equations. Imamura et al. [14] performed high-Reynolds-number flow simulations over an airfoil by the LBM with an incompressible model. Sun and Hsu [15,16] proposed the adaptive lattice Boltzmann model for compressible flows and calculated shock wave propagation, a flow over a cylinder, and a transonic flow over an airfoil cascade. Kataoka and Tsutahara [17] developed a compressible Euler model of the LBM and showed that the LBM can clearly capture discontinuity, such as a shock wave, in the calculation of the Riemann problem. The compressible fluid model of the LBM, however, tends to be more unstable than the incompressible one [18]. Cao et al. [18] proposed the finite difference lattice Boltzmann method (FDLBM), obtained by applying a standard finite difference (FD) scheme to the discrete Boltzmann equation. They proved that numerical stability can be improved by using an adequate FD scheme and a suitable Courant–Friedricks–Lewey condition. Tsutahara et al. [19] developed a new model of the FDLBM and carried out direct simulations of aeroacoustic problems by using the FDLBM, which is based on the second-order-accurate Runge–Kutta time integration and an explicit third-order-accurate upwind scheme. They showed that acoustic behavior can be well resolved in the direct simulation by the FDLBM with a smaller number of grids than the standard CAA scheme for a direct numerical simulation of aeroacoustic problems. Li et al. [20,21] proposed an LB model in which the collision term is modified to take into account the relaxation times associated with the intermolecular potential and the weak repulsive potential and calculated aeroacoustic problems using the proposed LB model. They also showed that the proposed LBM and the standard CAA scheme give identical results.

In the present study, we developed a numerical procedure based on the FDLBM for a more efficient and accurate numerical simulation of BVI phenomena and acoustic behaviors. To reduce the vortex dissipation, the perturbation approach is applied to the discrete Boltzmann equation, which is the governing equation of the FDLBM. The discretization of the governing equation is based on a second-order-accurate explicit Runge–Kutta time integration and a fifth-order-accurate upwind scheme that includes additional terms to capture shock waves clearly. Subsonic and transonic flows around an airfoil were simulated to validate the perturbed discrete Boltzmann equation system. Then, two-dimensional subsonic and transonic BVI problems were investigated. Although Lee and Bershader [3] investigated a mechanism of acoustic wave generation using numerical simulations of an airfoil-vortex

collision case, a mechanism of BVI noise generation was not fully investigated. Thus, the mechanism of the acoustic wave generation caused by BVI is discussed in this paper. The effect of the flow Mach number and influence of the vortex miss distance were also investigated.

II. Formulation

A. Governing Equations

First of all, we write down the governing equations for the conventional FDLBM for the compressible Euler model [17]. Then, the perturbation method will be introduced into the FDLBM. When t, x_α, and f_i represent, respectively, the time, the Cartesian coordinates, and the velocity distribution function of the ith particle, the governing equation is given by the following discrete Boltzmann equation (or discrete BGK equation):

$$\frac{\partial f_i}{\partial t} + c_{i\alpha}\frac{\partial f_i}{\partial x_\alpha} - \frac{A}{\phi}c_{i\alpha}\frac{\partial (f_i - f_i^{\mathrm{eq}})}{\partial x_\alpha} = -\frac{1}{\phi}(f_i - f_i^{\mathrm{eq}}) \qquad (i = 1, 2, \ldots, 9; \qquad \alpha = 1, 2) \tag{1}$$

where the subscripts i and α indicate, respectively, the kind of particles and the space direction in the Cartesian coordinates. A given positive constant, ϕ, is the relaxation time. $c_{i\alpha}$ is the particle velocity vector; $c_{i\alpha} = (0, 0)$ for $i = 1$, $c_{i\alpha} = (c_1 \cos \pi i/2, c_1 \sin \pi i/2)$ for $i = 2, 3, 4, 5$ and $c_{i\alpha} = \{c_2 \cos \pi(i/2 + 1/4), c_2 \sin \pi(i/2 + 1/4)\}$ for $i = 6, 7, 8, 9$. c_1 and c_2 are constants that represent the magnitude of the particle velocity. The equilibrium distribution function, f_i^{eq} in Eq. (1), is given by following equations [17]:

$$f_i^{\mathrm{eq}} = \rho\left(A_i + B_i\frac{u_\alpha c_{i\alpha}}{c_1^2} + D_i\frac{1}{c_1^4}u_\alpha c_{i\alpha}u_\beta c_{i\beta}\right) \tag{2}$$

where

$$A_i = \begin{cases} 2e(b-2)/\eta_0^2 bc_1^2 & i = 1 \\ [-c_2^2 + 2e\{c_2^2(b-2)/\eta_0^2 + 2\}/bc_1^2 + c_2^2 u_\alpha u_\alpha/c_1^4]/4(c_1^2 - c_2^2) & i = 2\text{–}5 \\ [-c_1^2 + 2e\{c_1^2(b-2)/\eta_0^2 + 2\}/bc_1^2 + u_\alpha u_\alpha/c_2^2]/4(c_2^2 - c_1^2) & i = 6\text{–}9 \end{cases}$$

$$B_i = \begin{cases} \{-c_2^2 + 2e(b+2)/bc_1^2 + u_\alpha u_\alpha/c_1^2\}/2c_1^2(c_1^2 - c_2^2) & i = 2\text{–}5 \\ \{-c_1^2 + 2e(b+2)/bc_1^2 + u_\alpha u_\alpha/c_1^2\}/2c_2^2(c_2^2 - c_1^2) & i = 6\text{–}9 \end{cases}$$

$$D_i = \begin{cases} 1/2c_1^4 & i = 2\text{–}5 \\ 1/2c_2^4 & i = 6\text{–}9 \end{cases}$$

where η_0 is a given constant. The constant b is associated with the specific-heat ratio γ by $b = 2/(\gamma - 1)$. The density ρ, the flow velocity u_α, and the internal energy e are defined as

$$\rho = \sum_i^9 f_i \qquad u_\alpha = \frac{1}{\rho}\sum_i^9 f_i c_{i\alpha} \qquad e = \frac{1}{\rho}\sum_i^9 f_i \frac{c_{i\alpha}^2 + \eta_i^2}{2} - \frac{1}{2}u_\alpha^2 \tag{3}$$

where η_i, which is introduced to control the specific-heat ratio, is given by $\eta_i = \eta_0$ for $i = 1$ and $\eta_i = 0$ for $i = 2, \ldots, 9$. The pressure p is given from the density and the internal energy by the equation of state for an ideal gas, $p = (\gamma - 1)\rho e$. The sound speed c_s is calculated by $c_s = \sqrt{\gamma(\gamma - 1)e}$. Third term on the left-hand side of Eq. (1) is an additional term that was introduced in [19]. According to the Chapman–Enskog expansion for small ϕ, the conventional discrete Boltzmann equation, which does not include the additional term, is equivalent to the Euler equations for compressible fluid with the error of $O(\phi)$. On the other hand, the stability condition for the present BGK collision term requires that the time increment, Δt, should be $\Delta t < \phi/2$. Therefore, a very small time increment must be chosen to keep the error small, which results in poor calculation efficiency. However, Eq. (1) with the additional term is equivalent to the compressible Euler equations with the error of $O(\phi - A)$. Therefore, we can use larger ϕ, keeping the error from the compressible Euler equations small by setting A close to ϕ. As a result, a larger time increment becomes usable, and the calculation will be more efficient (see [19] for details).

In this paper, inviscid transonic compressible flows are calculated using the FDLBM. However, it has been known that the calculations by the LBM or the FDLBM become unstable when the flow Mach number becomes large. To resolve this difficulty, we employ a moving grid technique. For example, if the flow around a stationary NACA 0012 airfoil is a uniform flow, the maximum value of the local Mach number is approximately 1.26 when the Mach number of the uniform flow is 0.8, and the calculation by the FDLBM becomes unstable. On the other hand, if the flow around the moving airfoil whose moving speed Mach number is 0.8 in fluid at rest, the local Mach number of the flow velocity will be $1.26 - 0.8 = 0.46$, and the calculation by the FDLBM will be stable. Because both problems are identical due to the Galilean invariance, we employ this technique to calculate transonic flows. We employ the arbitrary Lagrangian Eulerian (ALE) technique to apply moving boundary condition to a surface of the airfoil. Then, the governing equation of the ALE-formulated FDLBM [22] becomes

$$\frac{\partial f_i}{\partial t} + (c_{i\alpha} - V_\alpha)\frac{\partial f_i}{\partial x_\alpha} - \frac{A}{\phi}c_{i\alpha}\frac{\partial (f_i - f_i^{eq})}{\partial x_\alpha} = -\frac{1}{\phi}(f_i - f_i^{\mathrm{eq}}) \qquad (i = 1, 2, \ldots, 9; \qquad \alpha = 1, 2) \tag{4}$$

where the variable V_α is the grid velocity vector. Because we consider the translation of the moving grid only and do not consider the deformation of the grid, V_α becomes the moving speed of the airfoil. In this paper, Eq. (4) is used for the calculations.

B. Perturbation Approach

To reduce the numerical dissipation of a vortex, which is the most prominent difficulty of a numerical simulation of BVI phenomena, the perturbation approach is introduced into the discrete BGK equation (4). In this approach, the solution, f_i, of Eq. (4) and the macroscopic variables ρ, u_α, and e are decomposed into two parts as follows:

$$f_i = f_{V,i} + f_{P,i}, \qquad \rho = \rho_V + \rho_P,$$
$$u_\alpha = u_{V,\alpha} + u_{P,\alpha}, \qquad e = e_V + e_P \tag{5}$$

where $f_{V,i}$, ρ_V, $u_{V,\alpha}$, and e_V are the prescribed parts that satisfy Eqs. (2–4) and the compressible Euler equations. $f_{P,i}$, ρ_P, $u_{P,\alpha}$, and e_P are the remaining parts that are obtained from the perturbed governing equation. The solution, $f_{V,i}$, of the prescribed part is associated with the macroscopic variables ρ_V, $u_{V,\alpha}$, and e_V by Eq. (3). Similarly, the total solution, $f_{V,i} + f_{P,i}$, is connected with the total macroscopic variables $\rho_V + \rho_P$, $u_{V,\alpha} + u_{P,\alpha}$, and $e_V + e_P$ by Eq. (3). After deducting Eq. (3) for the prescribed solution from Eq. (3) for the total solution, the equations that associate the solution, $f_{P,i}$, of the remaining part with the macroscopic variables ρ_P, $u_{P,\alpha}$ and e_P are obtained as follows:

$$\rho_P = \sum_i^9 f_{P,i}$$
$$u_{P,\alpha} = \frac{1}{(\rho_V + \rho_P)} \sum_i^9 f_{P,i} c_{i\alpha} - \frac{\rho_P u_{V,\alpha}}{\rho_V + \rho_P}$$
$$e_P = \frac{1}{(\rho_V + \rho_P)} \left\{ \sum_i^9 f_{P,i} \frac{c_{i\alpha}^2 + \eta_i^2}{2} + \rho_V \left(e_V + \frac{u_{V,\alpha}^2}{2} \right) \right\} - e_V - \frac{1}{2}(u_{V,\alpha} + u_{P,\alpha})^2 \tag{6}$$

Substitute Eq. (5) into Eq. (4). Because the solution, $f_{V,i}$, of the prescribed part satisfies Eq. (4), the following perturbed equation is obtained:

$$\frac{\partial f_{P,i}}{\partial t} + (c_{i\alpha} - V_\alpha) \frac{\partial f_{P,i}}{\partial x_\alpha} - \frac{A}{\phi} c_{i\alpha} \frac{\partial (f_{P,i} - f_{P,i}^{\mathrm{eq}})}{\partial x_\alpha} = -\frac{1}{\phi}(f_{P,i} - f_{P,i}^{\mathrm{eq}}) \tag{7}$$

where

$$f_{P,i}^{\mathrm{eq}} = f_i^{\mathrm{eq}}(\rho_V + \rho_P, u_{V,\alpha} + u_{P,\alpha}, e_V + e_P) - f_i^{\mathrm{eq}}(\rho_V, u_{V,\alpha}, e_V) \tag{8}$$

Consequently, the obtained perturbed discrete BGK equations are composed of Eqs. (6–8). The desired macroscopic solutions $\rho_V + \rho_P$, $u_{V,\alpha} + u_{P,\alpha}$, and $e_V + e_P$ are obtained from Eq. (6). The prescribed parts ρ_V, $u_{V,\alpha}$, and e_V are given by an analytical model, such as the Scully vortex [23]. The perturbed solution, $f_{P,i}$, is calculated by Eq. (7). To use the boundary fitted finite difference grid, Eq. (7) in the Cartesian coordinates is transformed into that on the generalized coordinate, ξ_α:

$$\frac{\partial f_{P,i}}{\partial t} + (c_{i\alpha} - V_\alpha) \frac{\partial \xi_\beta}{\partial x_\alpha} \frac{\partial f_{P,i}}{\partial \xi_\beta} - \frac{A}{\phi} c_{i\alpha} \frac{\partial \xi_\beta}{\partial x_\alpha} \frac{\partial (f_{P,i} - f_{P,i}^{\mathrm{eq}})}{\partial \xi_\beta} = -\frac{1}{\phi}(f_{P,i} - f_{P,i}^{\mathrm{eq}}) \tag{9}$$

It is well understood that the boundary condition of a perfect fluid is the slip condition. The slip condition of a moving body is given by $u_n = V_n$, where u_n and V_n denote the normal flow velocity and the normal velocity of a moving body on the boundary. Thus, the slip condition of the unknown part is given as

$$u_{P,n} = V_n - u_{V,n} \tag{10}$$

To solve Eq. (9) numerically, the remaining macroscopic variables on the boundary are required. As in Sun and Hsu [16], they are determined by the symmetric condition, $\partial u_t / \partial n = 0$, $\partial \rho / \partial n = 0$, and $\partial e / \partial n = 0$, where u_t denotes the tangential flow velocity on the boundary. The remaining macroscopic variables of the unknown part are given as follows:

$$\frac{\partial u_{P,t}}{\partial n} = -\frac{\partial u_{V,t}}{\partial n}, \qquad \frac{\partial \rho_P}{\partial n} = -\frac{\partial \rho_V}{\partial n}, \qquad \frac{\partial e_P}{\partial n} = -\frac{\partial e_V}{\partial n} \tag{11}$$

where $u_{P,t}$ and $u_{V,t}$ are the tangential flow velocities of the remaining part and the prescribed part on the boundary, respectively. After calculating the unknown variables on the boundary from Eqs. (10) and (11), the corresponding equilibrium distribution function, $f_{P,i}^{\mathrm{eq}}$, is determined by Eq. (8). Then, the distribution function $f_{P,i}$ on the boundary is obtained by $f_{P,i} = f_{P,i}^{\mathrm{eq}} + f_{P,i}^{\mathrm{neq}}$, where $f_{P,i}^{\mathrm{neq}}$ is the nonequilibrium distribution function on the boundary and is calculated by an extrapolation from adjacent fluid.

C. Discretizations

The discrete BGK equation (9) is spatially discretized by the FD scheme. Although Tsutahara et al. [19] demonstrated a direct numerical simulation of an aeroacoustic problem by a third-order-accurate upwind scheme, the conventional third-order-accurate upwind scheme has the tendency to generate undesirable wiggles caused by its truncation error with respect to the fifth-order derivatives in the neighborhood of a shock wave. Thus, the governing Eq. (9) is discretized by a fifth-order-accurate upwind scheme [24] that includes the dissipative term to reduce numerical oscillations. When the convectional terms of Eq. (9) and a grid point number are represented by $c_\xi \partial g / \partial \xi$ and a subscript j, the fifth-order-accurate upwind scheme containing the dissipative term is shown as

$$c_\xi \left. \frac{\partial g}{\partial \xi} \right|_j = c_\xi \frac{-2g_{j-3} + 15g_{j-2} - 60g_{j-1} + 20g_j + 30g_{j+1} - 3g_{j+2}}{60\Delta\xi} - \kappa |c_\xi| \frac{g_{j-1} - 2g_j + g_{j+1}}{\Delta\xi}$$
$$c_\xi > 0$$
$$c_\xi \left. \frac{\partial g}{\partial \xi} \right|_j = c_\xi \frac{-3g_{j-2} - 30g_{j-1} - 20g_j + 60g_{j+1} - 15g_{j+2} + 2g_{j+3}}{60\Delta\xi} - \kappa |c_\xi| \frac{g_{j-1} - 2g_j + g_{j+1}}{\Delta\xi}$$
$$c_\xi < 0 \tag{12}$$

where

$$\kappa = \tau \frac{|p_{j-1} - 2p_j + p_{j+1}|}{|p_{j-1} + 2p_j + p_{j+1}|}$$

The positive constant τ controls the strength of the dissipative effect. The pressure p is calculated from the total density, $\rho_V + \rho_P$, and the total internal energy, $e_V + e_P$, by the equation of state. This approach is based on the one proposed by Jameson et al. [25,26]. A first-order-accurate upwind scheme and a third-order-accurate upwind scheme are employed at the grid points that are adjacent to the boundary. The discretized governing equation is advanced in time by using a second-order-accurate explicit Runge–Kutta time integration.

The governing equation (9) is normalized by the particle speed c_1, the chord length c, and the density of the rest fluid ρ_0. The remaining particle speed c_2 and η_0 are set for 3.0 and 2.0, which are recommended values for a stable calculation [15]. To set the specific ratio for 1.4, the constant b is given as $b = 5.0$. The calculation by the FDLBM becomes more stable when the particle speed c_1 and the sound speed $c_s = \sqrt{\gamma(\gamma - 1)e_0}$, where e_0 indicates the internal energy of the rest fluid, are identical. Thus, the internal energy of the rest fluid e_0 is given by $e_0 = 1/(\gamma(\gamma - 1)) = 25.0/14.0$. As mentioned, the error between the governing equations and the compressible Euler equations are $O(\phi - A)$. To reduce this error, $\phi - A$ is set for a very small value. The effect of $\phi - A$ is shown in Fig. 2a. The numerical result was found to be converged if we set $\phi - A < 1.0 \times 10^{-5}$. Thus, $\phi - A$ was set for 1.0×10^{-7}. Because the BGK collision term requires $\Delta t < \phi/2$, the relaxation time ϕ is set for the same order as the time increment Δt. As a result, ϕ and A were set for $0.005 + 1.0 \times 10^{-7}$ and 0.005, respectively. Figure 2b shows the effect of τ. The result shows that the undesirable wiggles

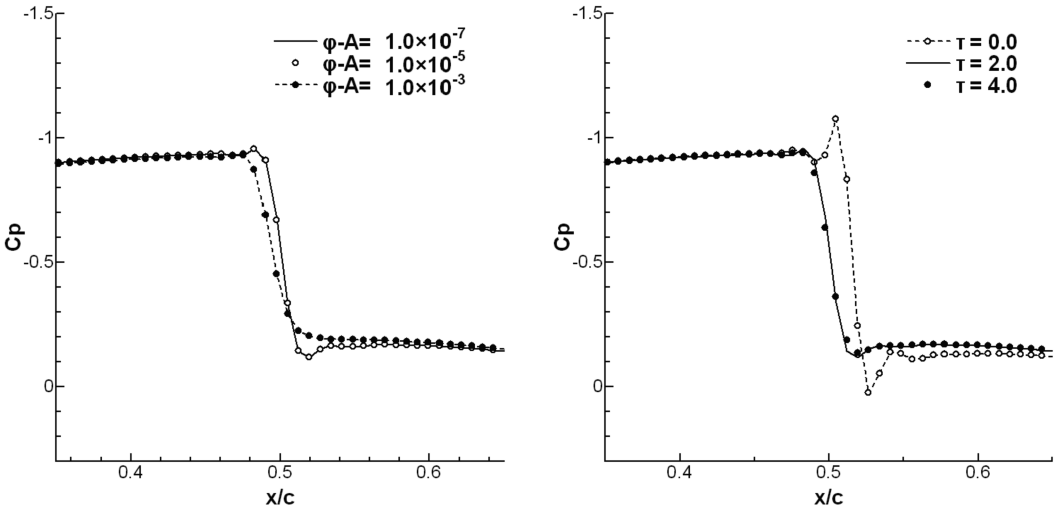

Fig. 2 Close-up of a shock wave profile in a flow over a NACA airfoil at $\alpha_0 = 0$ deg and $M = 0.8$: a) influence of $\phi - A$, and b) influence of τ.

around the shock wave vanish if we set $\tau = 2.0$. Therefore, τ is set for 2.0.

III. Validation of the Present Method

In this section, the proposed numerical procedure is tested with several numerical simulations of subsonic and transonic flows around an airfoil with and without a vortex. First, the present method is compared with other numerical methods based on the discretization of the Euler equations in a simulation of a flow around an airfoil without a vortex. Then, the proposed numerical procedure is validated in a BVI calculation. The grid and time increment dependence are also investigated in both simulations.

A. Simulations of Flows Around an Airfoil

The numerical simulation of the flow over the airfoil with a NACA 0012 section has been performed to validate the present numerical procedure. A 301 (chordwise) × 101 (normal) body fitted grid (O grid) was employed for this calculation. The size of the computational domain extends 10 chord lengths in all directions from the surface of the airfoil. The sponge region where the grid resolution gradually becomes lower is located at outside of the computational domain so that the reflections from the artificial exterior boundary are reduced. The sponge region containing 301 × 11 node points extends 20 chord lengths from the joint between the computational region and the sponge region. The airfoil surface boundary condition is the slip boundary condition defined by Eqs. (10) and (11). Because the fluctuations generated from the flow around the airfoil are presumed to dissipate well in the sponge region, the macroscopic variables on the exterior boundary are given as constants. The airfoil moves with uniform speed in a rest fluid. The macroscopic variables of the rest fluid are given as the prescribed parts ρ_V, $u_{V,\alpha}$, and e_V in Eq. (5). The calculation was continued until the numerical solutions reach steady state. The time increment of this simulation was prescribed to be 0.00125.

We evaluated grid and time increment dependence of the calculation before comparing the obtained results with other numerical data. The angle of attack and the Mach number of the moving speed are represented as α_0 and M, respectively. The evaluation was performed in the calculation at $\alpha_0 = 0$ deg and $M = 0.8$. Figure 3a shows the time increment dependence of the calculation. Both results became perfectly identical because the solution is steady. The grid dependence is shown in Fig. 3b. The three calculations were almost the same, but the resolution of the shock wave profiles in the calculation with the coarse mesh was poor compared with the others. The calculation with the present mesh was practically identical to the finer calculation, including the shock wave profiles. Thus, the time increment is set for 0.00125 and the present mesh is employed in the following numerical simulations.

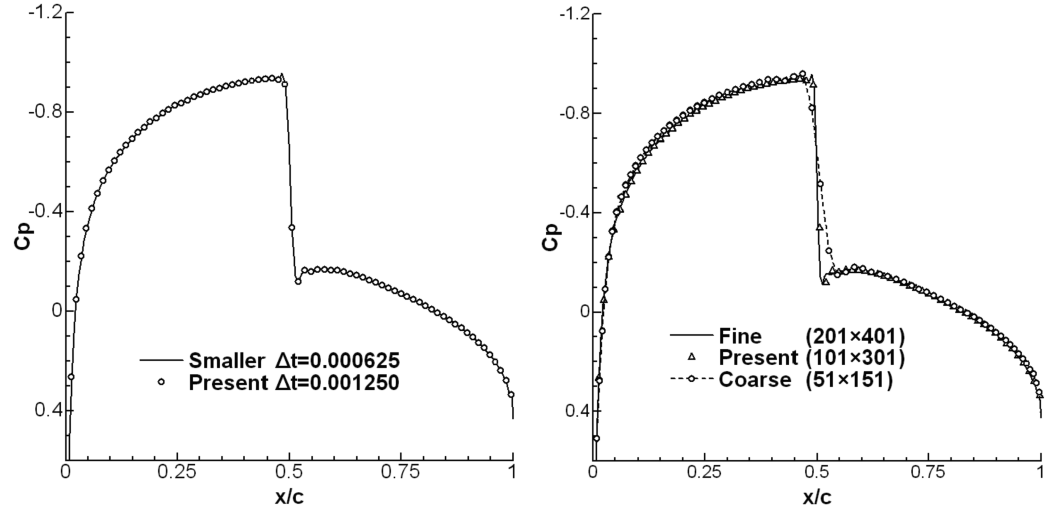

Fig. 3 Evaluation of numerical accuracy in a simulation without a vortex: a) time increment dependence, and b) grid dependence.

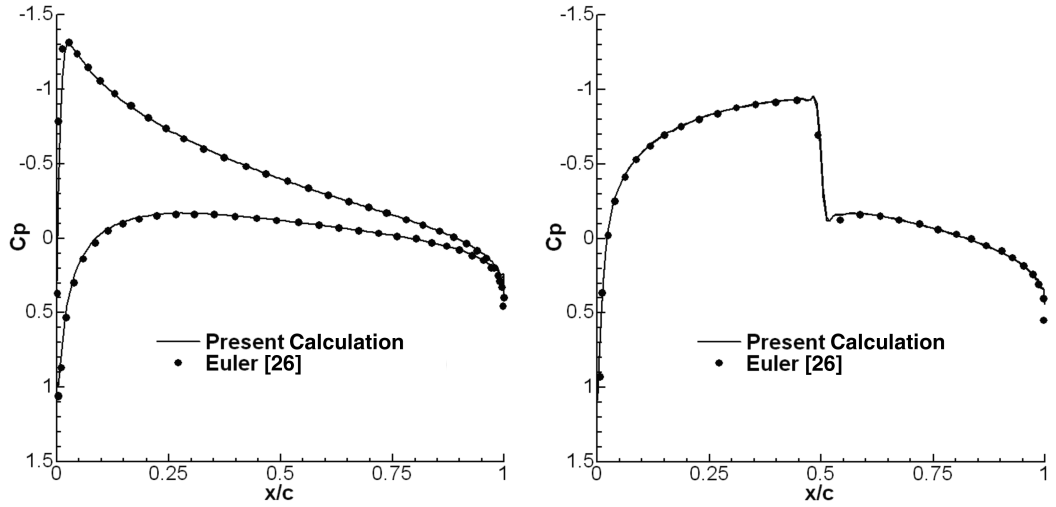

Fig. 4 Comparison of the surface pressure distributions of NACA 0012 airfoil: a) $\alpha_0 = 3$ deg and $M = 0.5$, and b) $\alpha_0 = 0$ deg and $M = 0.8$.

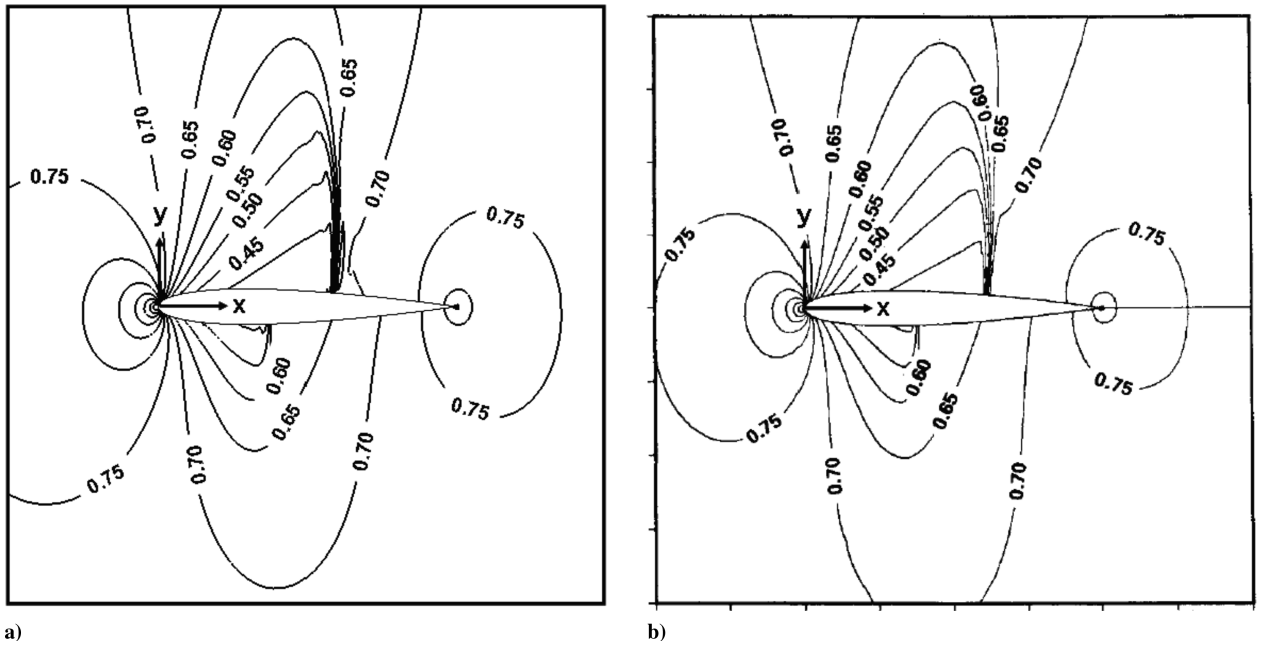

Fig. 5 Comparison of pressure contour lines at $\alpha_0 = 1.25$ deg and $M = 0.8$: a) present calculation, and b) Pulliam [27].

The surface pressure distributions at $\alpha_0 = 3$ deg and $M = 0.5$ and at $\alpha_0 = 0$ deg and $M = 0.8$ are shown in Figs. 4a and 4b. Good agreements between the present numerical results and another numerical one [26] were obtained. It was also shown that the proposed numerical procedure can capture shock waves clearly. This is because the FDLBM is one kind of kinetic CFD scheme, generally with smaller numerical dissipations than conventional CFD solvers based on the macroscopic governing equations, including Euler equation solvers. We emphasize this feature as one of the merits of the FDLBM or the LBM. A comparison of pressure contour lines at $\alpha_0 = 1.25$ deg and $M = 0.8$ is shown in Fig. 5. The strong shock wave on the upper surface and the weak shock wave on the lower surface were simulated clearly by the proposed numerical method. The obtained numerical result shows the same pressure patterns as the result of the Euler calculation based on an artificial dissipation model [27]. Consequently, these results proved that the present numerical method based on the FDLBM is suitable for the calculation of an inviscid compressible flow.

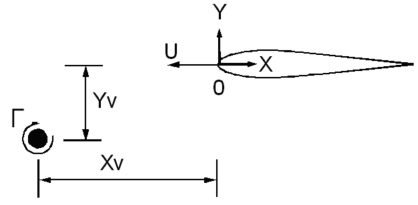

Fig. 6 Definitions of the coordinate system and parameters of the two-dimensional BVI (from [3]).

B. Simulations of Blade-Vortex Interactions

A transonic BVI problem was calculated by the present numerical procedure, and its results were compared with other numerical methods for BVI calculations [4,7,8,10]. Figure 6 shows the definitions of the coordinate system and the parameters of the two-dimensional BVI problem. The NACA 0012 airfoil moves with uniform speed U in a rest fluid and interacts with a vortex, which is analytically given by the Scully vortex model [23]. Its tangential velocity distribution is defined by following equation:

$$v_\theta = (\Gamma/2\pi r)\{r^2/(r^2 + a^2)\} \tag{13}$$

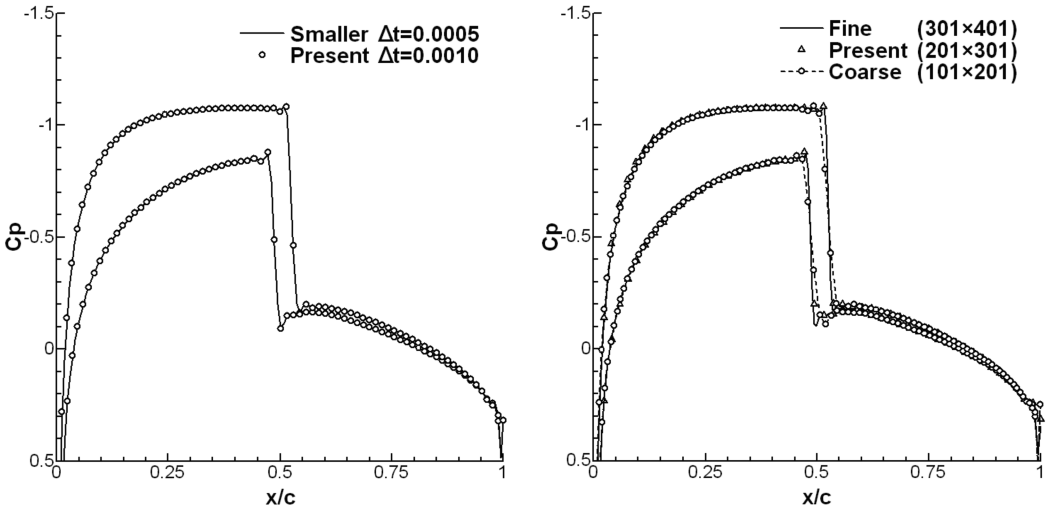

a) b)

Fig. 7 Evaluation of numerical accuracy in the BVI calculation ($M = 0.8$, $a = 0.05$, $\Gamma = -0.2$, $X_v = 0.0$, and $Y_v = -0.26$): a) time increment dependence, and b) grid dependence.

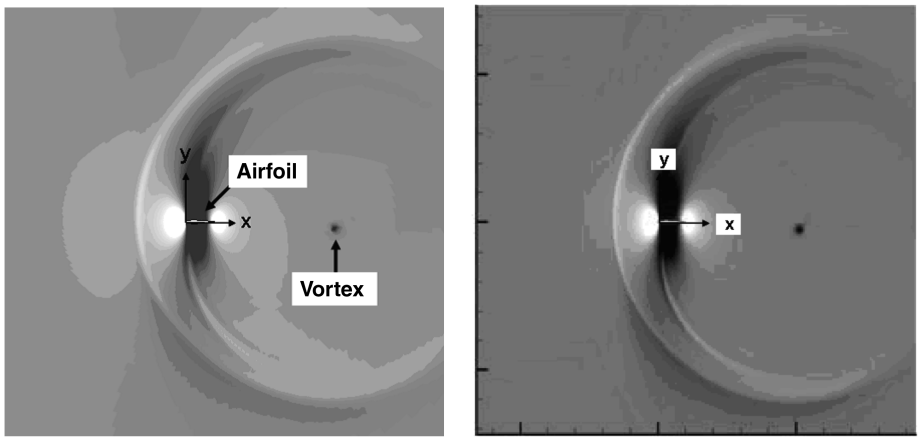

a) b)

Fig. 8 Comparison of the instantaneous pressure contour ($M = 0.8, a = 0.05, \Gamma = -0.2, X_v = 5.0$, and $Y_v = -0.26$): a) present calculation, and b) Wie et al. [8].

where a and r denote the core radius and the radial distance from the vortex center. The vortex strength is represented as Γ. The counterclockwise vortex is defined as positive. The pressure and density fields induced by the vortex are determined by the radial momentum equation in conjunction with the energy equation for constant enthalpy flows. The Mach number M of the moving speed U and the miss distance Y_v are prescribed to be 0.8 and -0.26, respectively. The vortex parameters are given as $a = 0.05$ and

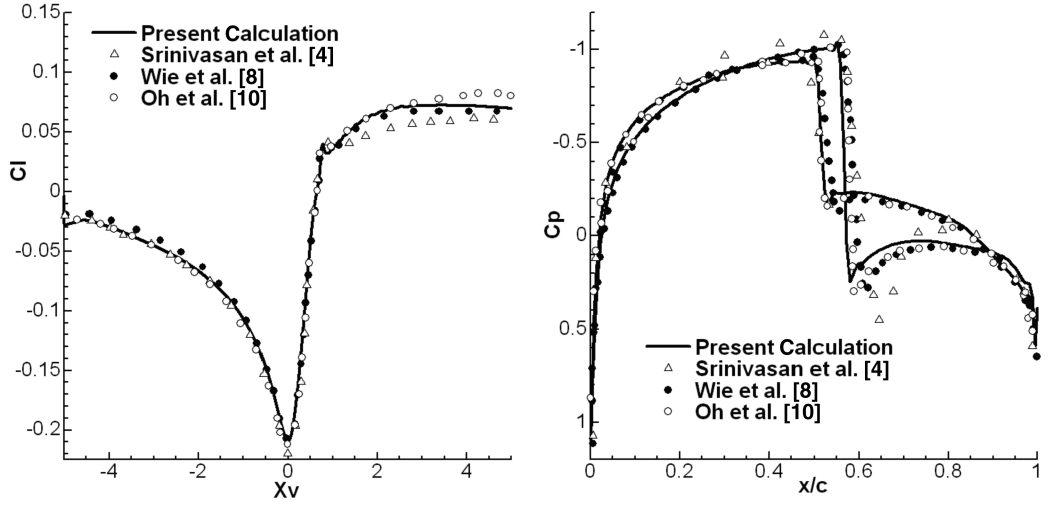

a) b)

Fig. 9 Comparison of the lift variation and instantaneous surface pressure distribution during BVI ($M = 0.8$, $a = 0.05$, $\Gamma = -0.2$, and $Y_v = -0.26$): a) lift coefficient variation, and b) instantaneous surface pressure when a vortex is located at $X_v = 1.0$.

$\Gamma = -0.2$, where Γ is normalized by the chord length c and the uniform speed U. The 301×201 body fitted grid (O grid) was employed for the simulation of the BVI problem. The computational domain has $10c$ in all directions from the surface of the airfoil. The sponge region that has 301×16 grid points is located at the outside of the computational domain. The size of the sponge region is $15c$ in all directions from the joint between itself and the computational domain. The slip condition is applied as the airfoil surface boundary condition. The macroscopic variables on the exterior boundary are given as constants, as in Sec. III.A. The prescribed components in Eq. (5) are given by the solutions of the Scully vortex defined by Eq. (13). Firstly, the steady solution of the flow without a vortex is calculated, and then the Scully vortex is introduced at the place of $X_v = -5.0$ and $Y_v = -0.26$. The BVI calculation was started from this flowfield and was continued while the relative distance X_v between the vortex center and the leading edge changes from $-5c$ to $5c$. The time step of this simulation was prescribed to be 0.001. The numerical simulation of the BVI was performed by 12,500 time steps, and the total elapsed computational time was approximately 2.0 h on a personal computer with a Pentium4, 2.66 GHz processor.

The grid and time increment dependence of the present numerical method is investigated in the BVI calculation. The time increment dependence is shown in Fig. 7a. Both results were identical, although the BVI calculation is an unsteady one. The grid dependence is shown in Fig. 7b. The three calculations became almost same except for the shock wave profiles. The shock waves are dull in the coarse mesh calculation due to a lack of grid resolution. The calculation with the present mesh thoroughly agreed with the finer calculation, including the shock wave profiles. Thus, the time increment is set for 0.001 and the present mesh is employed in the BVI calculations.

Figure 8 shows a comparison of the instantaneous pressure contour with the CAA calculation [8], which shows the propagation of BVI noise when the vortex is located at $X_v = 5.0$. Figure 8b is the numerical result obtained by the CAA solver [8] developed by combining a perturbation method with an OHOC scheme. In the simulation by this CAA method, the multiblock grid that has 123,410 nodes was used [8]. Our result shows the same pattern of noise propagation as that of the CAA method, although the number of grid points is smaller than that of the CAA method. The lift variation and surface pressure distribution were compared with those of the prescribed vortex method [4], the perturbation method [8], and the adaptive mesh method [10]. The time history of the lift coefficient is shown in Fig. 9a. It was observed that the initial lift coefficient is a negative value because of the downwash of the clockwise vortex. As the vortex approaches the leading edge, the lift coefficient decreases gradually. When the vortex reaches a position nearest to the leading edge, the lift coefficient becomes the negative maximum value. After that, the lift coefficient rises rapidly. This characteristic is the same as that obtained by the other numerical simulations [4,8,10]. The instantaneous airfoil surface pressure distribution when the vortex is located at $X_v = 1.0$ is shown in Fig. 9b. Migrations of the shock waves caused by the existence of the vortex were observed. The current result agreed with the others very well. As with the simulations without the vortex, the present numerical method was also found to have the ability to capture shock waves clearly, although the number of grid points is smaller than that of the CAA method [8]. In Fig. 10, the instantaneous surface pressure distributions were compared with those obtained by other perturbation methods [4,7]. Good agreements were obtained between the present results and the other methods.

IV. Results of Blade-Vortex Interaction Simulations and Discussion

In this section, three BVI calculations were performed by the present FDLBM to investigate the generation mechanism of the BVI noise, the effect of flow Mach number, and the effect of the vortex miss distance. The computational grid, domain, and time increment were described in Sec. III.B. First, the mechanism of the BVI noise generation is discussed in a transonic BVI calculation. Then, a subsonic BVI calculation is carried out to investigate the effect of the flow Mach number. Finally, the effect of the vortex miss distance is researched in a transonic BVI calculation with a large vortex miss distance.

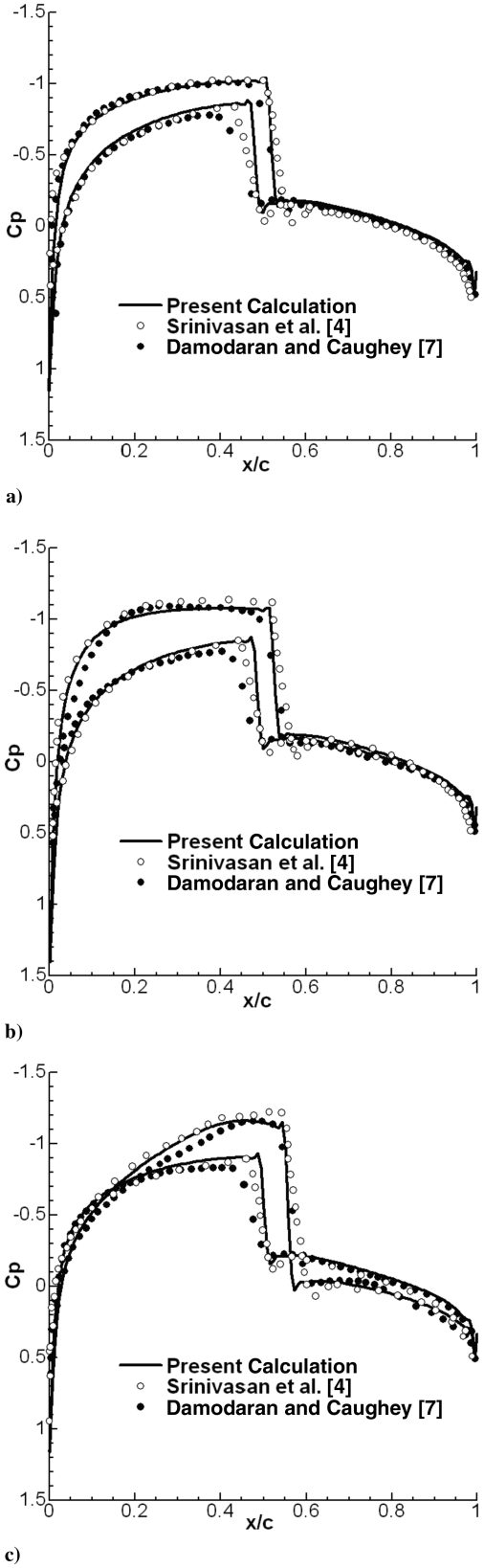

Fig. 10 Comparison of the instantaneous surface pressure distributions during BVI ($M = 0.8$, $a = 0.05$, $\Gamma = -0.2$, and $Y_v = -0.26$) when a vortex is located at a) $X_v = -0.5$, b) $X_v = 0.0$, and c) $X_v = 0.5$.

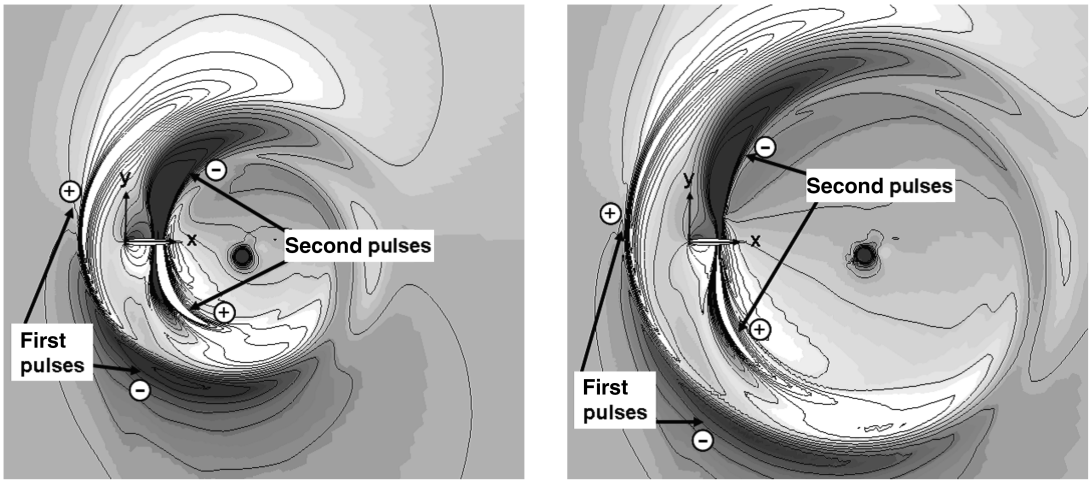

a) b)

Fig. 11 Instantaneous fluctuation pressure distributions of BVI noise ($M = 0.8$, $a = 0.05$, $\Gamma = -0.2$, and $Y_v = -0.26$) when a vortex is located at a) $X_v = 2.0$, and b) $X_v = 3.0$.

A. Mechanism of Blade-Vortex Interaction Noise Generation

To investigate the mechanism of the BVI noise generation, a transonic BVI calculation is implemented at $M = 0.8$, $a = 0.05$, $\Gamma = -0.2$, and $Y_v = -0.26$. To recognize the generation and propagation of acoustic waves caused by the BVI, the fluctuation pressure Δp is defined by $\Delta p = p - p_0$, where p_0 denotes the pressure of the steady state without the vortex. Figure 11 shows the instantaneous fluctuation pressure distributions when the vortex is located at $X_v = 2.0$ and $X_v = 3.0$. The acoustic wave propagations are captured well in this calculation. First, a positive pressure pulse and a negative pressure pulse are emitted from the upper surface and the lower surface, respectively. After a short time, another set of

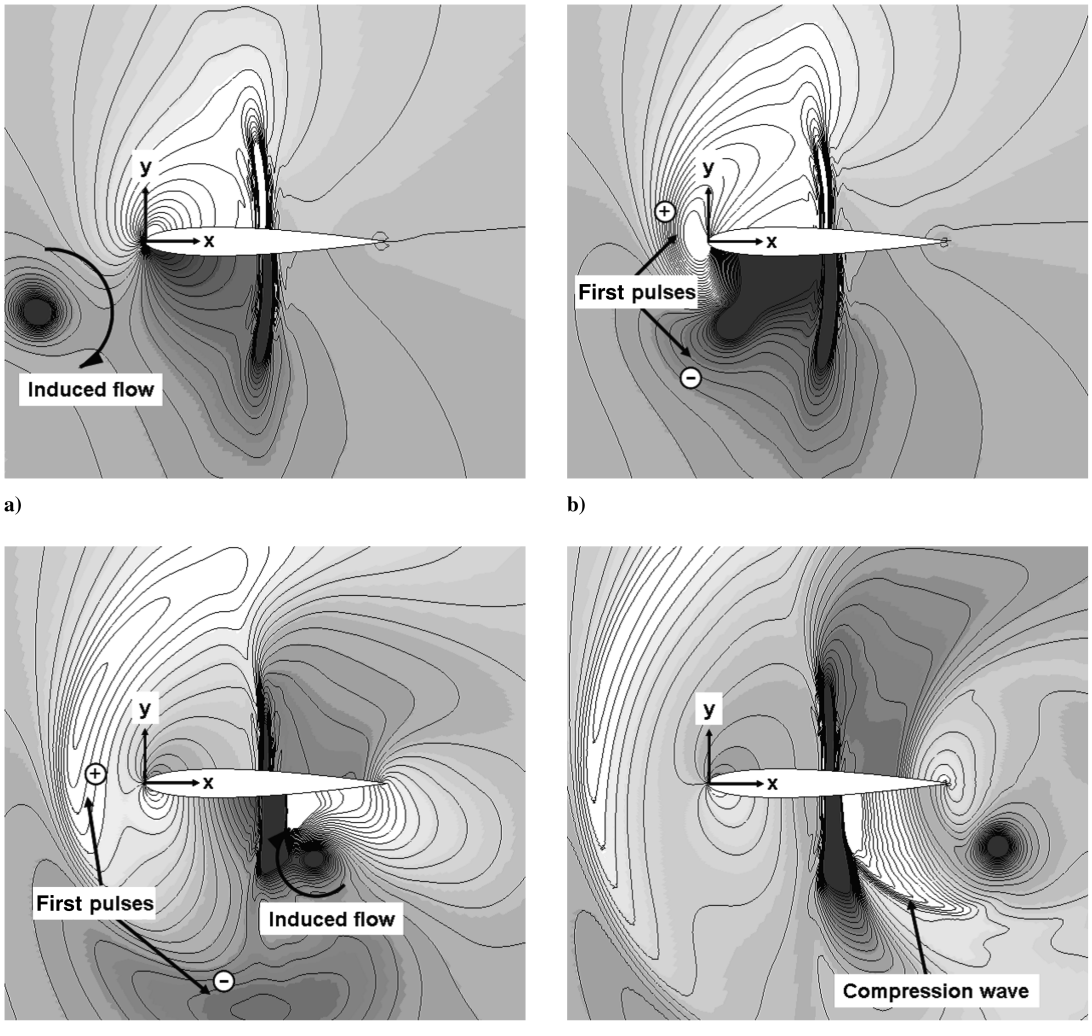

a) b)

c) d)

Fig. 12 Instantaneous fluctuation pressure distributions during BVI ($M = 0.8$, $a = 0.05$, $\Gamma = -0.2$, and $Y_v = -0.26$) when a vortex is located at a) $X_v = -0.4$, b) $X_v = 0.2$, c) $X_v = 0.7$, and d) $X_v = 1.2$.

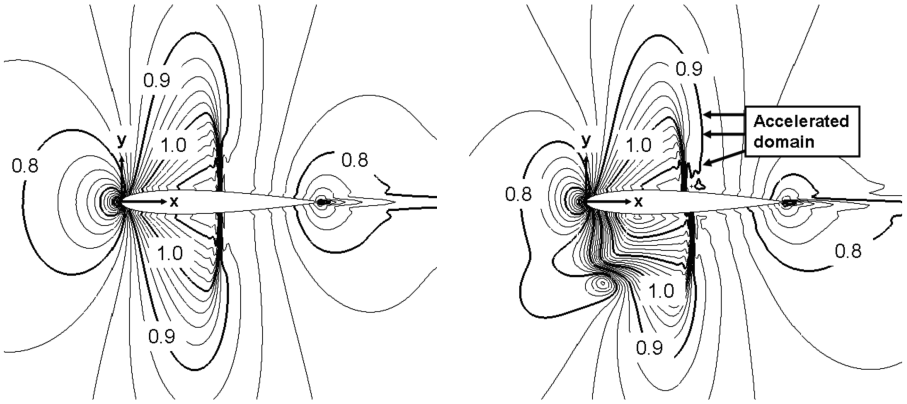

a) b)

Fig. 13 Instantaneous local Mach number distributions ($M = 0.8$, $a = 0.05$, $\Gamma = -0.2$, and $Y_v = -0.26$) when a vortex is located at a) $X_v = -5.0$, and b) $X_v = 0.2$. The contour levels are from $M_{\text{local}} = 0.0$ to 1.5.

pressure pulses with opposite signs are observed. The instantaneous fluctuation pressure distributions around the airfoil are shown in Fig. 12. The vortex induces a clockwise flow due to its negative vorticity. As the vortex approaches the leading edge, the pressure rises near the upper surface and reduces near the lower surface (Fig. 12a), because the induced flow impinges on the upper surface. These pressure fluctuations are emitted from the airfoil as acoustic waves after the vortex passes near the leading edge. When the vortex is just behind the shock wave on the lower side, a rapid pressure rise takes place (Fig. 12c), because the induced flow impinges the lower surface behind the shock wave. This strong compression wave is observed as the acoustic wave emitted from the lower surface. To investigate a sound source of the negative pressure pulse radiated from the upper surface, the instantaneous local Mach number M_{local} distributions are shown in Fig. 13. The local Mach number is calculated from the relative flow velocity Δu_α defined by $\Delta u_\alpha = u_\alpha - U$, where u_α and U denote the flow velocity and the uniform speed of the airfoil, respectively. When the vortex goes into the supersonic region on the lower side (Fig. 13b), it is clearly observed that the flow velocity behind the shock wave on the upper side increases more than that in the flowfield, which is not influenced by the vortex (Fig. 13a). The pressure reduction caused by this increment of the flow velocity behind the shock wave seems to be a sound source of the negative pressure pulse. The expansion wave, generated by the interaction between the vortex and the supersonic domain around the leading edge, seems to increase the flow velocity behind the shock wave, but that detail is not yet clear.

B. Effect of Flow Mach Number

In this section, a subsonic BVI problem at $M = 0.4$ was simulated with the normalized vortex parameters of $a = 0.05$, $\Gamma = -0.2$, and $Y_v = -0.26$ to investigate the effect of the flow Mach number. Figure 14 displays the instantaneous fluctuation pressure distributions when the vortex is located at $X_v = 1.5$ and $X_v = 3.0$. The acoustic wave propagations are captured well in this calculation also. First, pressure pulses in both sides propagate in the same way as the results of the transonic BVI calculation. Then, another set of pressure pulses with opposite signs propagate from the same surfaces. The wave patterns of the subsonic BVI noise are different from those of the transonic BVI noise. The instantaneous fluctuation pressure distributions around the airfoil are shown in Fig. 15. The vortex induces a clockwise flow due to its negative vorticity. As the vortex approaches the leading edge, the pressure rises near the upper surface and reduces near the lower surface (Fig. 15a), because the induced flow impinges on the upper surface. After the vortex passes near the leading edge, these pressure fluctuations are emitted as acoustic waves from the airfoil (Fig. 15b). When the vortex is under the airfoil, the pressure increases near the lower surface and decreases near the upper surface because of the impingement of the induced flow (Fig. 15c). Then, they propagate as the acoustic waves (Fig. 15d).

C. Effect of Vortex Miss Distance

The last numerical simulation was performed at $M = 0.8$, $a = 0.05$, $\Gamma = -0.2$, and $Y_v = -0.78$. In this simulation, the miss

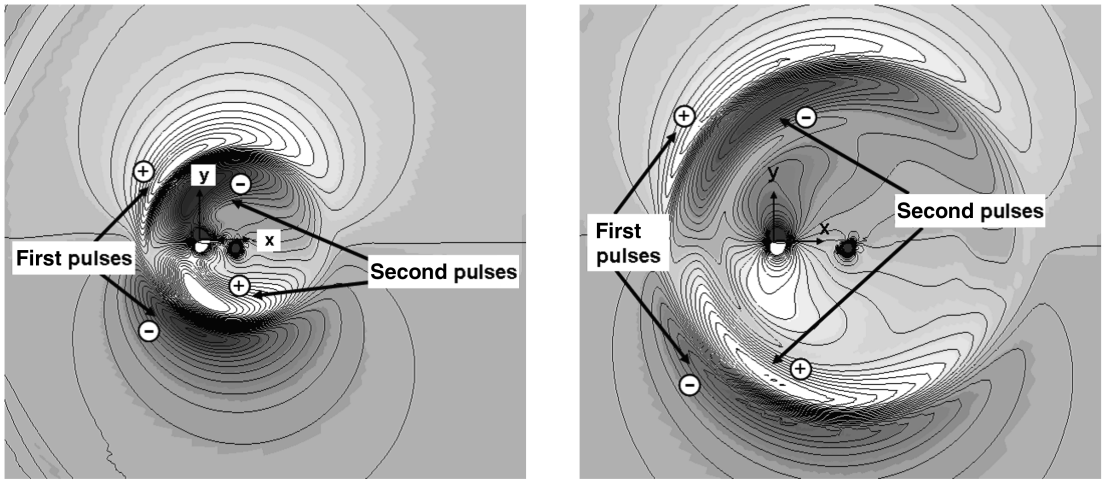

a) b)

Fig. 14 Instantaneous fluctuation pressure distributions of BVI noise ($M = 0.4$, $a = 0.05$, $\Gamma = -0.2$, and $Y_v = -0.26$) when a vortex is located at a) $X_v = 1.5$, and b) $X_v = 3.0$.

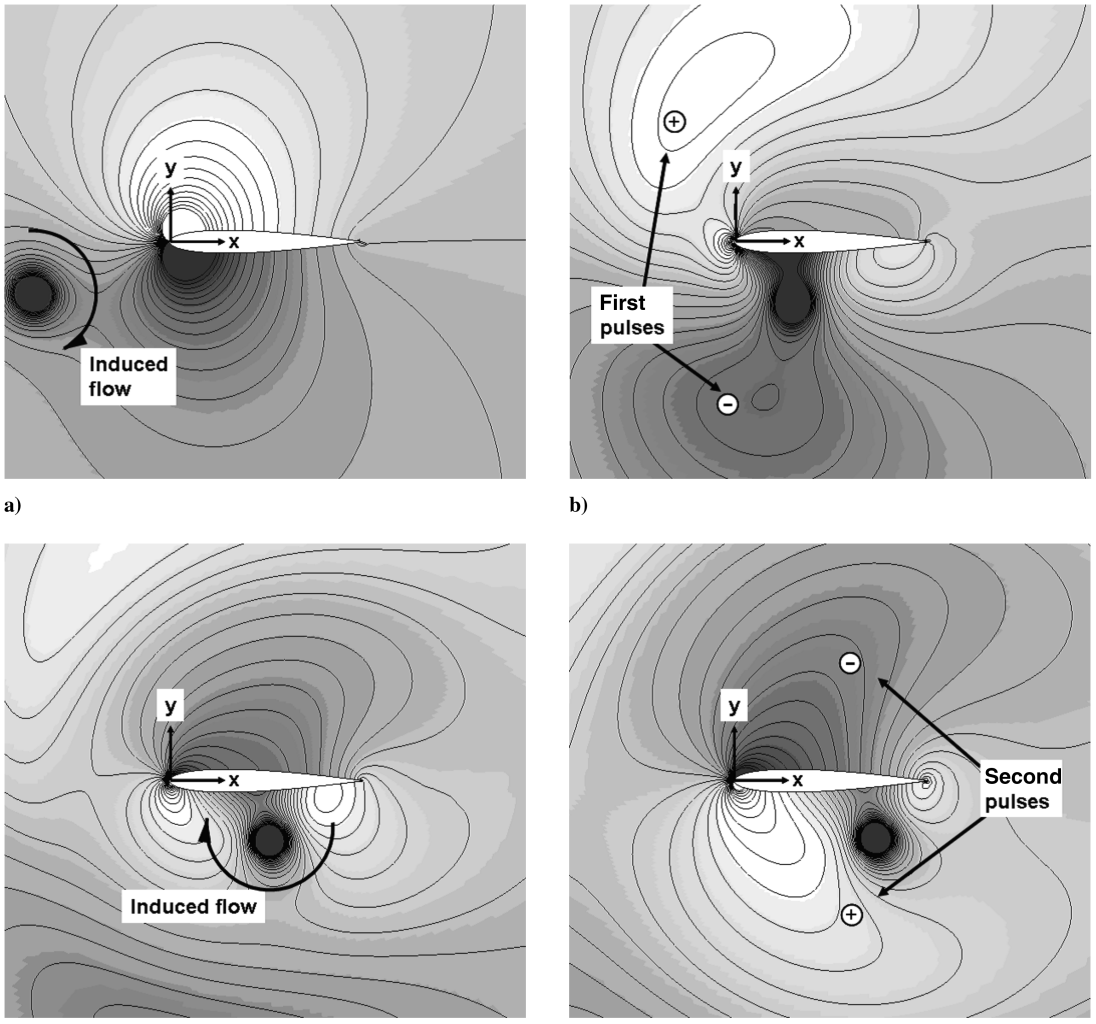

Fig. 15 Instantaneous fluctuation pressure distributions during BVI ($M = 0.4$, $a = 0.05$, $\Gamma = -0.2$, and $Y_v = -0.26$) when a vortex is located at a) $X_v = -0.7$, b) $X_v = 0.3$, c) $X_v = 0.5$, and d) $X_v = 0.7$.

distance Y_v was expanded to 3 times as long as that of the first simulation, which was carried out at $M = 0.8$, $a = 0.05$, $\Gamma = -0.2$, and $Y_v = -0.26$. The instantaneous fluctuation pressure distributions are shown in Fig. 16. The wave patterns of the generated pressure pulses are similar to those of the first simulation. However, the positive pressure pulse, generated on the lower surface after the propagation of the first pressure pulses, is emitted later than that of the first simulation. The instantaneous fluctuation pressure distributions around the airfoil are shown in Fig. 17. First, a positive pressure pulse and a negative pressure pulse are generated by the

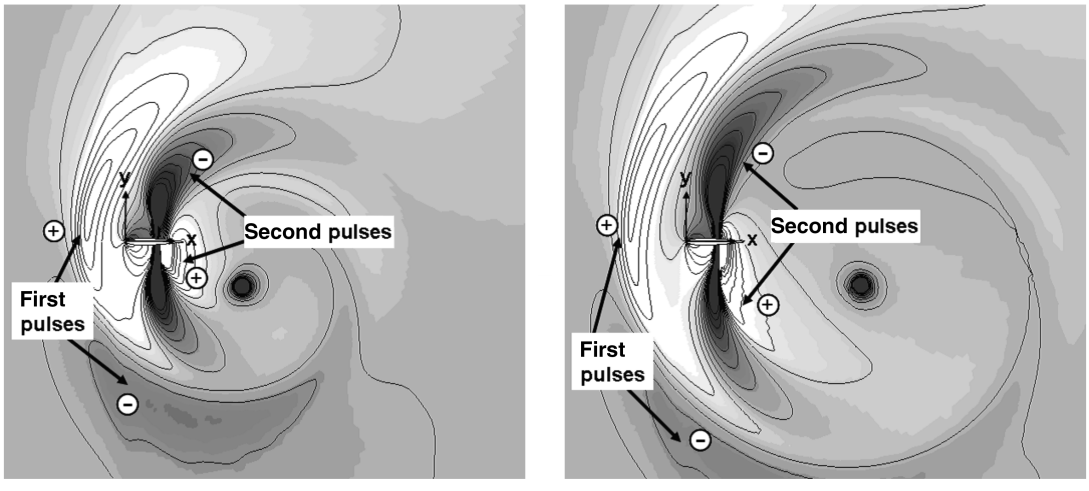

Fig. 16 Instantaneous fluctuation pressure distributions of BVI noise ($M = 0.8$, $a = 0.05$, $\Gamma = -0.2$, and $Y_v = -0.78$) when a vortex is located at a) $X_v = 2.0$, and b) $X_v = 3.0$.

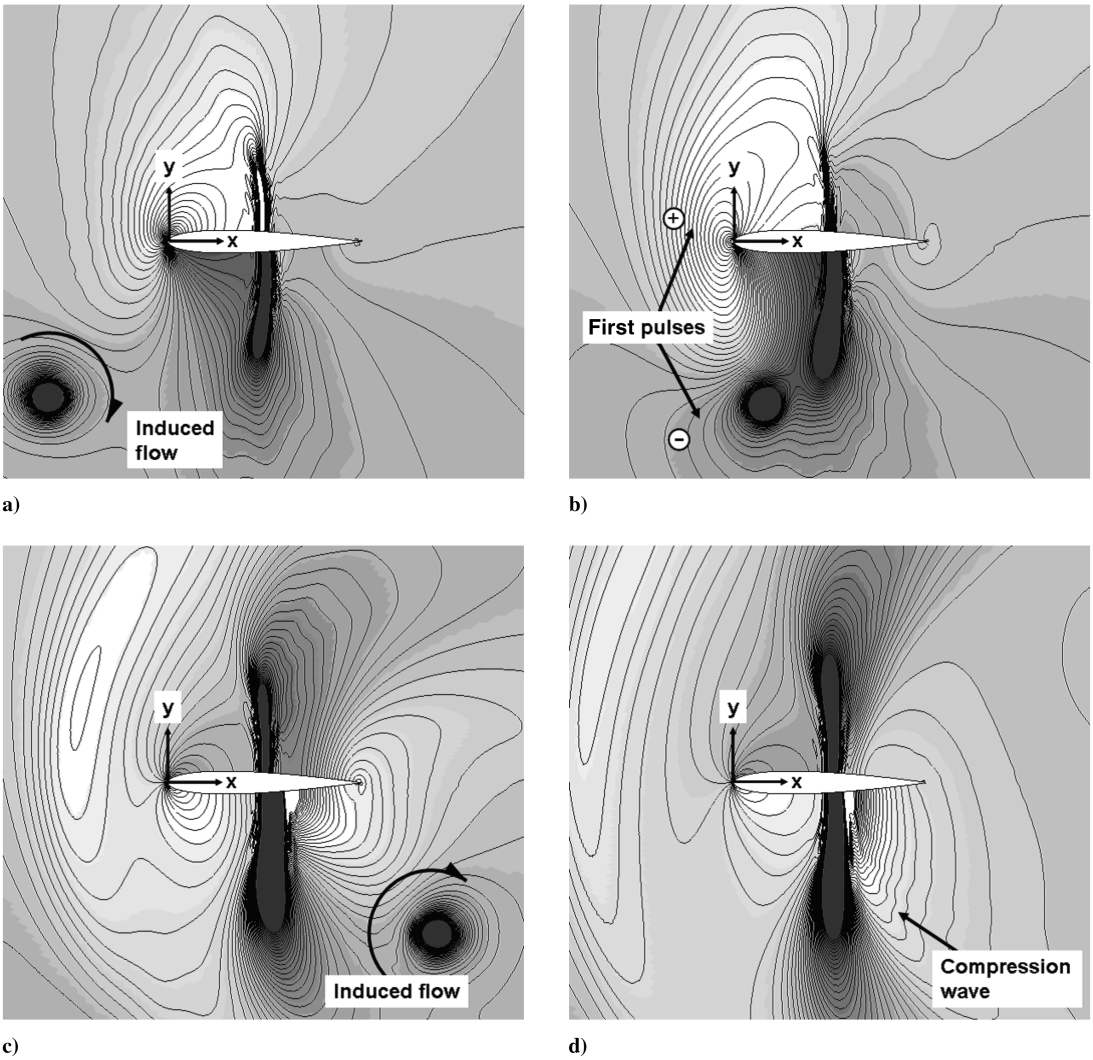

Fig. 17 Instantaneous fluctuation pressure distributions during BVI ($M = 0.8$, $a = 0.05$, $\Gamma = -0.2$, and $Y_v = -0.78$) when a vortex is located at a) $X_v = -0.6$, b) $X_v = 0.2$, c) $X_v = 1.4$, and d) $X_v = 2.3$.

same generated by the same phenomenon as the former calculation in Sec. IV.A that was performed at a small miss distance $Y_v = -0.26$ (Fig. 17c). Next, a positive pressure pulse is generated on the lower surface after the vortex leaves from under the airfoil completely (Fig. 17d). The positive pressure pulse of the second simulation is, however, produced when the vortex is under the trailing edge. This difference is caused by the difference of an intersection angle between a direction of the induced flow and a tangential direction of the lower surface behind the shock wave. In this calculation, the induced flow is almost parallel to the lower surface when the vortex is under the trailing edge. As the vortex leaves from under the trailing edge, the intersection angle between the direction of the induced flow and the tangential direction of the lower surface becomes large. Then, the induced flow impinges the lower surface behind the shock wave. As a result, a compression wave is generated and emitted from the lower surface.

V. Conclusions

The FDLBM for the BVI problem has been developed by introducing a perturbation method into the discrete BGK equation. For a validation of the present numerical method, subsonic and transonic flows around an airfoil without a vortex have been demonstrated. Good agreement has been obtained between the current results and those of other numerical methods. Numerical results of the two-dimensional transonic BVI simulation performed by the proposed method were compared with other numerical methods. The obtained results show that the present numerical method has the ability to capture shock waves clearly and to resolve acoustic waves well with a smaller number of grid points than that of the CAA solver based on a perturbation method. The total elapsed computational time was only 2.0 h on a personal computer. To investigate the mechanism of the BVI noise generation as well as the effect of the flow Mach number the vortex miss distance, three BVI calculations have been carried out. In the transonic BVI case, the first pressure pulses are generated by the impingement of the induced flow on the leading edge. A second pressure pulse emitted from the lower side of the airfoil is generated by the impingement of the induced flow on a lower surface behind a shock wave. In the subsonic BVI case, an impingement of induced flow on a leading edge of the airfoil causes acoustic wave generation. It was also found that the vortex miss distance influences the interval between the first pressure pulses and the second pressure pulses.

References

[1] Booth, E. R., Jr., "Experimental Observation of Two-Dimensional Blade-Vortex Interaction," *AIAA Journal*, Vol. 28, No. 8, 1990, pp. 1353–1359. doi:10.2514/3.25225

[2] Kalkhoran, I. N., and Wilson, D. R., "Experimental Investigation of the Parallel Blade-Vortex Interaction at Transonic Speeds," *AIAA Journal*, Vol. 30, No. 8, 1992, pp. 2087–2092. doi:10.2514/3.11183

[3] Lee, S., and Bershader, D., "Head-On Parallel Blade-Vortex Interaction," *AIAA Journal*, Vol. 32, No. 1, 1994, pp. 16–22. doi:10.2514/3.11945

[4] Srinivasan, G. R., McCroskey, W. J., and Kutler, P., "Numerical Simulation of the Interaction of a Vortex with Stationary Airfoil in Transonic Flow," AIAA Paper 84-0254, Jan. 1984.
[5] Srinivasan, G. R., McCroskey, W. J., and Baeder, J. D., "Aerodynamics of Two-Dimensional Blade-Vortex Interaction," *AIAA Journal*, Vol. 24, No. 10, 1986, pp. 1569–1576. doi:10.2514/3.9486
[6] Srinivasan, G. R., and McCroskey, W. J., "Euler Calculations of Unsteady Interaction of Advancing Rotor with a Line Vortex," *AIAA Journal*, Vol. 31, No. 9, 1993, pp. 1659–1666. doi:10.2514/3.49095
[7] Damodaran, M., and Caughey, D. A., "Finite Volume Calculation of Inviscid Transonic Airfoil-Vortex Interaction," *AIAA Journal*, Vol. 26, No. 11, 1988, pp. 1346–1353. doi:10.2514/3.10046
[8] Wie, S. Y., Cho, C. H., and Lee, D. J., "Numerical Investigation About Blade Vortex Interaction Using Vortex Embedded CAA Method," Acoustical Society of Korea Paper 502, June 2006.
[9] Hwang, C. J., and Kuo, J. Y., "Adaptive Finite Volume Upwind Approaches for Aeroacoustic Computations," *AIAA Journal*, Vol. 35, No. 8, 1997, pp. 1286–1293.
[10] Oh, W. S., Kim, J. S., and Kwon, O. J., "Numerical Simulation of Two-Dimensional Blade-Vortex Interactions Using Unstructured Adaptive Meshes," *AIAA Journal*, Vol. 40, No. 3, 2002, pp. 474–480.
[11] Qian, Y. H., D'Humieres, D., and Lallemand, P., "Lattice BGK Models for Navier-Stokes Equation," *Europhysics Letters*, Vol. 17, No. 6, 1992, pp. 479–484. doi:10.1209/0295-5075/17/6/001
[12] Chen, H., Chen, S., and Mattheus, W. H., "Recovery of the Navier-Stokes Equations Using a Lattice-Gas Boltzmann Method," *Physical Review A*, Vol. 45, No. 8, 1992, pp. R5339–R5342. doi:10.1103/PhysRevA.45.R5339
[13] Chen, S., and Doolen, G. D., "Lattice Boltzmann Method for Fluid Flows," *Annual Review of Fluid Mechanics*, Vol. 30, Jan. 1998, pp. 329–364. doi:10.1146/annurev.fluid.30.1.329
[14] Imamura, T., Suzuki, K., Nakamura, T., and Yoshida, M., "Flow Simulation Around an Airfoil by Lattice Boltzmann Method on Generalized Coordinates," *AIAA Journal*, Vol. 43, No. 9, 2005, pp. 1968–1973. doi:10.2514/1.7554
[15] Sun, C., "Adaptive Lattice Boltzmann Model for Compressible Flows: Viscous and Conductive Properties," *Physical Review E (Statistical Physics, Plasmas, Fluids, and Related Interdisciplinary Topics)*, Vol. 61, No. 3, 2000, pp. 2645–2653. doi:10.1103/PhysRevE.61.2645
[16] Sun, C., and Hsu, A. T., "Three-Dimensional Lattice Boltzmann Model for Compressible Flows," *Physical Review E (Statistical Physics, Plasmas, Fluids, and Related Interdisciplinary Topics)*, Vol. 68, No. 1, 2003, pp. 016303.1–016303.14.
[17] Kataoka, T., and Tsutahara, M., "Lattice Boltzmann Method for the Compressible Euler Equations," *Physical Review E (Statistical Physics, Plasmas, Fluids, and Related Interdisciplinary Topics)*, Vol. 69, No. 5, 2004, pp. 056702.1–056702.14. doi:10.1103/PhysRevE.69.056702
[18] Cao, N., Chen, S., Jin, S., and Martinez, D., "Physical Symmetry and Lattice Symmetry in the Lattice Boltzmann Method," *Physical Review E (Statistical Physics, Plasmas, Fluids, and Related Interdisciplinary Topics)*, Vol. 55, No. 1, 1997, pp. R21–R24. doi:10.1103/PhysRevE.55.R21
[19] Tsutahara, M., Kataoka, T., Shikata, K., and Takada, N., "New Model and Scheme for Compressible Fluids of the Finite Difference Lattice Boltzmann Method and Direct Simulations of Aerodynamic Sound," *Computers and Fluids*, Vol. 37, No. 1, Jan. 2008, pp. 79–89. doi:10.1016/j.compfluid.2005.12.002
[20] Li, X. M., Leung, R. C. K., and So, R. M. C., "One-Step Aeroacoustics Simulation Using Lattice Boltzmann Method," *AIAA Journal*, Vol. 44, No. 1, 2006, pp. 78–89. doi:10.2514/1.15993
[21] Li, X. M., So, R. M. C., and Leung, R. C. K., "Propagation Speed, Internal Energy, and Direct Aeroacoustics Simulation Using Lattice Boltzmann Method," *AIAA Journal*, Vol. 44, No. 12, 2006, pp. 2896–2903. doi:10.2514/1.18933
[22] Tamura, A., and Tsutahara, M., "Direct Simulation of Acoustic Waves Emitted from Moving Bodies by the Finite Difference Lattice Boltzmann Method," AIAA Paper 2006-2489, 2006.
[23] Scully, M. P., "Computation of Helicopter Rotor Wake Geometry and Its Influence on Rotor Harmonic Loads," Aeroelastic and Structures Research Laboratory, Massachusetts Inst. of Technology, TR-178-1, Boston, MA, 1975.
[24] Rai, M. M., and Moin, P., "Direct Numerical Simulation of Transition and Turbulence in a Spatially Evolving Boundary Layer," *Journal of Computational Physics*, Vol. 109, No. 2, Dec. 1993, pp. 169–192. doi:10.1006/jcph.1993.1210
[25] Jameson, A., "Solution of the Euler Equations for Two-Dimensional Transonic Flow by a Multigrid Method," *Applied Mathematics and Computation*, Vol. 13, Nos. 3–4, 1983, pp. 327–356. doi:10.1016/0096-3003(83)90019-X
[26] Jameson, A., Schmidt, W., and Turkel, E., "Numerical Solutions of the Euler Equations by Finite Volume Method Using the Runge-Kutta Timestepping Schemes," AIAA Paper 81-1259, 1981.
[27] Pulliam, T. H., "Artificial Dissipation Models for the Euler Equations," *AIAA Journal*, Vol. 24, No. 12, 1986, pp. 1931–1940. doi:10.2514/3.9550

X. Zhong
Associate Editor